Soliton crystals in Kerr resonators

Daniel C. Cole [1,2]*, Erin S. Lamb [1], Pascal Del'Haye [1,3], Scott A. Diddams[1] and Scott B. Papp[1]

Self-organized solitons confined to an optical resonator would offer unique capabilities for experiments in communication, computation and sensing with light. Here, we report the observation of soliton crystals in monolithic Kerr microresonators— spontaneously and collectively ordered ensembles of co-propagating solitons whose interactions discretize their allowed temporal separations. We unambiguously identify and characterize soliton crystals through analysis of their 'fingerprint' optical spectra, which arise from spectral interference between the solitons. We identify a rich space of soliton crystals exhibiting crystallographic defects and we perform time-domain measurements to directly confirm our inference of their crystal structure. Soliton crystallization is explained by long-range soliton interactions mediated by resonator mode degeneracies, and we probe the qualitative difference between soliton crystals and the disorganized soliton liquid that would form in the absence of these interactions. Our work explores the physics of monolithic Kerr resonators in a regime of dense soliton occupation and offers a way to increase the efficiency of Kerr combs. Furthermore, the extreme degeneracy of the configuration space of soliton crystals suggests an implementation for an on-chip optical buffer.

Optical solitons have recently found a new realization in frequency combs generated in passive, monolithic Kerr-nonlinear resonators[1] (microcombs). These microcombs are a major step forward in frequency-comb technology[2], because they enable the generation of combs in platforms with low size, weight and power requirements. When a continuous-wave (c.w.) pump laser is coupled into a whispering-gallery mode of a high-Q Kerr resonator, broad optical spectra are generated through cascaded four-wave mixing. With appropriate power and laser-resonator frequency detuning, the resulting fields modelock to form circulating dissipative Kerr-cavity solitons[3–10]. These solitons are pulsed excitations on top of a non-zero c.w. background, and have robust deterministic properties that may be tailored through resonator design[11,12] and tuned in real-time through manipulation of the pump laser. Microcombs based on solitons extend the range of accessible comb repetition rates and provide a route towards chip-integrated self-referenced comb technology.

Single solitons and ensembles of several co-propagating solitons have been reported in Kerr resonators constructed from a variety of crystalline and amorphous materials[3–7], with repetition rates ranging from 22 GHz (ref. [6]) to 1 THz (ref. [7]). Formally equivalent to monolithic Kerr resonators are lower-repetition-rate fibre-loop resonators, where the generation and control of soliton ensembles has recently been explored experimentally[13–16]. These systems are described by a driven and damped nonlinear Schrödinger equation known as the Lugiato–Lefever equation (LLE) within the field of microcombs. This equation supports stationary nonlinear periodic wave solutions variously known as primary comb, cnoidal waves and Turing patterns, and also supports localized soliton-like solutions[8,9,17–19]. Numerical studies of related quasi-c.w.-pumped fibre-loop resonators[20–22] have characterized the stationary and non-stationary nonlinear wave arrays that form spontaneously through modulation instability[20]. An analogy to the states of matter presented in these studies has subsequently been extended to other systems including, for example, single-pass nonlinear fibre systems[23] and the harmonically mode-locked fibre laser[24,25], where a mechanism of soliton crystallization specific to that laser system was identified that is based on two different timescales of the laser gain medium[26].

In this Article, we present an observation of and model for soliton crystallization in passive, monolithic Kerr resonators. The soliton crystals we have observed are self-organized ensembles of independent, particle-like excitations, which fill the angular domain of the resonator. These ensembles exhibit a rich configuration space supporting various crystallographic defects[27], including vacancies (Schottky defects), shifted pulses (Frenkel defects) and periodicity over multiple scales (superstructure). These defects present evidence that soliton crystals are distinct from primary comb, and the crystallization mechanism that we have identified is different from the basic nonlinear dynamics of the system that lead to the well-known primary comb and spatiotemporal chaos (also known as modulation-instability comb)[8–10,28] solutions. In contrast with soliton crystals, primary comb and spatiotemporal chaos are extended patterns from which constituent pulses cannot be isolated and which are not degenerate with single solitons in the microcomb power-detuning phase plane[8].

Soliton crystals introduce a new regime of soliton physics into the field of microcombs. In passive c.w.-pumped ring resonator systems, solitons exhibit locally attractive interactions at small separations that culminate in pair annihilation or merger[14,29]. Thus, without, for example, manipulation of the pump laser to control these interactions[30], it has so far only been possible to observe sparsely populated ensembles of well-separated solitons in experiment. In contrast, soliton crystals consist of tightly packed solitons that fully occupy the resonator and exhibit novel collective temporal ordering. Crystallization of Kerr solitons manifests in our experiments as distinctive 'fingerprint' optical spectra arising from spectral interference between interacting solitons. Similar spectra have been previously reported, but until now have remained unexplained[31,32].

A series of physical effects supported by the resonator itself are responsible for soliton crystals and differentiate them from previously reported single- and multisoliton microcombs. First, because the solitons are tightly packed, a soliton crystal has an intracavity optical power similar to the spatiotemporal chaos that precedes it in the experiment and that fills the angular domain of the resonator[3,8]. Hence, soliton crystals form stably through adiabatic pump-laser frequency scans, without a need for the complex techniques used

in other demonstrations of Kerr solitons to avoid dissipation of the solitons due to thermal changes. Second, destructive soliton collisions are eliminated through a naturally arising collective soliton interaction mediated by an extended background wave in the cavity. This wave is the result of interference between the pump laser and excess light of a different frequency that is present due to spectrally localized enhancement of conversion efficiency caused by an avoided mode crossing in the resonator spectrum.
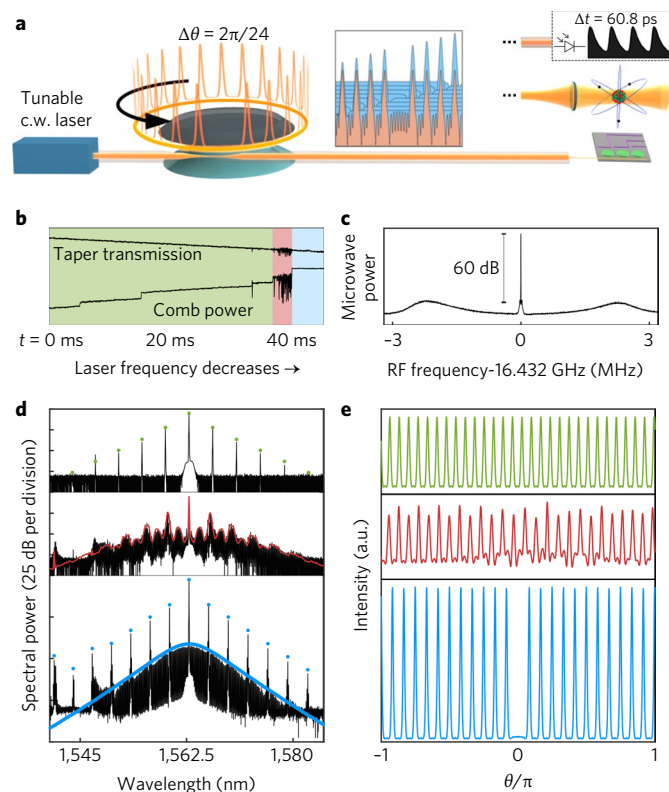
Results

Adiabatic generation of soliton crystals. We generated soliton crystals in silica Kerr whispering-gallery-mode resonators with free spectral ranges (FSRs) of ~26 GHz (ref. [33]) and ~16.4 GHz (ref. [34]) and anomalous dispersion. Our experimental procedure is depicted in Fig. 1a. A tapered optical fibre provides evanescent coupling of a ~30 mW telecommunications-band pump laser into a resonator whispering-gallery mode and couples out the generated Kerr-soliton-crystal frequency comb. Emerging from the resonator is a pulse train with highly ordered temporal separations between

Fig. 1 | Generation of a soliton crystal using the Kerr nonlinearity in a χ$^{(3)}$-nonlinear medium (here silica). a, Depiction of the generation and measurement of a crystal. Inset: plot on a logarithmic scale of the summation of many single soliton waveforms to yield a crystal with strong background oscillation. Right: possible applications of the system in radiofrequency (RF) waveform generation, spectroscopy and integrated photonics. **b,** Taper transmission and comb power during crystal generation. A thermal shift of the resonance leads to the non-Lorentzian taper transmission profile. Three regimes are visible: primary comb (green), chaos (red) and crystal (blue). **c,** A narrow measured RF beat indicates crystallization. **d,** Progression of experimental optical spectra (black) through the three regimes, with simulations (colour). The range of each plot is 100 dB. **e,** Simulated time-domain waveforms corresponding to the optical spectra plotted in **d**, plotted against the angular coordinate in a co-rotating frame (arbitrary vertical scale).

pulses, which we explore in detail throughout the remainder of this Article.

We formed soliton crystals by using a slowly decreasing pump laser frequency scan from 'blue' to 'red' laser-cavity detuning that terminated after the soliton comb was initiated[3]. This is similar to the experimental procedure that we reported previously for the generation and characterization of phase-locked microcombs[31,32], for which a frequency-domain description has recently been developed[35]. To explore the process of Kerr-soliton-crystal formation, we recorded the optical power transmitted through the tapered fibre during the laser frequency scan, as shown in Fig. 1b. By optically filtering the pump-laser frequency, we also measured the intensity of new comb light generated by four-wave mixing. The characteristic sawtooth shape of the resonance is due to thermal bistability effects[36]. Three qualitatively different regimes can be identified in these traces: (1) formation of initial primary comb[8–10,28], (2) the chaotic waveform preceding the crystal, and (3) the Kerr soliton crystal. The continuity or near continuity of the taper transmission during the transition from chaos to crystal contrasts with the dramatic 'soliton steps' that have been reported previously[3,6]. This indicates that the intracavity optical power of the crystal is similar to that of the chaos, which enables the generation and stabilization of the crystals through arbitrarily slow scans of the pump laser's frequency (for example, we are able to generate soliton crystals by adjusting the pump laser's frequency by tuning the voltage across a piezoelectric crystal by hand over several seconds). We observe behaviour consistent with a low-noise frequency comb following transition to the Kerr crystal, not only through the fibre-taper transmission and comb-intensity signals, but also in the microwave repetition frequency signal obtained by photodetection of the entire comb (Fig. 1c).

The most striking aspect of Kerr crystals is their optical spectra, which feature dramatic line-by-line intensity variations due to multiple-soliton interference. Figure 1d presents measurements (black traces) delineating a particular progression from primary comb to chaotic comb to crystal for the prototypical Kerr crystal in the bottom panel, which is composed of a train of 24 solitons evenly separated in time with a single vacancy. Here, the optical spectrum can be understood as the destructive interference between a tightly packed train of 24 solitons circulating the cavity, which yields the prominent comb lines spaced by 24 resonator FSRs, and a single, out-of-phase soliton that both 'fills in' the spectrum and produces the vacancy in the time domain. We modelled these spectra to obtain predictions for their intracavity intensity pattern (Fig. 1e) using the spatiotemporal LLE[8]. The numerical results, colour-coded to indicate the primary comb, chaotic and crystal regimes, have an accuracy demonstrated by agreement with experiment over the wide logarithmic-scale variations of the spectra. We note, however, that although both single solitons and few-soliton ensembles are steady-state solutions to the LLE, the 23-soliton crystal in Fig. 1d is not. When it is evolved under the LLE, the solitons exhibit attractive interactions and pairwise annihilation (see Supplementary Section VI). In fact, none of the crystals we present are stable solutions of the LLE, but they are solutions to a perturbed LLE with an altered dispersion term, as described in the following section.

Mechanism of Kerr soliton crystallization. The key to understanding why soliton crystals exist can be seen in their spectra. We observe excess Kerr comb generation relative to the expected hyperbolic-secant spectrum (not shown), for example, 6 dB near 1,547 nm and 18 dB near 1,541 nm in Fig. 1d, due to accidental degeneracies of the resonator mode family that supports our combs and other mode families. Such mode crossings lead to a dispersive change in the comb–resonator frequency detuning about the crossing, either increasing or decreasing the efficiency of comb formation. Mode crossing phenomena have been discussed previously:

in anomalous-dispersion resonators they can inhibit the formation of Kerr solitons[4,6], whereas they can facilitate the formation of Kerr combs in normal-dispersion resonators[37]. In our work in the anomalous-dispersion regime, mode crossings play a critical role in stabilizing attractive interactions within tightly packed, multiple-soliton ensembles. Formally, the result of a mode crossing is the incorporation of an extended background wave into the soliton waveform circulating in the resonator. This wave corresponds to the interference of excess light with the pump laser. When several of these perturbed solitons co-propagate in a resonator, they interact through their extended waves and arrange themselves such that the waves constructively interfere. Each soliton then lies at the peak of an extended background wave in the resonator, similar to predictions for bichromatically pumped Kerr combs[38]. Importantly, temporal separations between solitons are therefore required to be multiples of this wave's period, and the wave stabilizes the crystal against the attractive interactions discussed above. Furthermore, the wave's amplitude, and thus the strength of the crystal against perturbations, increases with the number of co-propagating perturbed solitons. Finally, we note that a mode crossing that predominantly affects a single frequency comb mode leads, effectively, to the injection of a single c.w. laser into the cavity waveform, giving this interaction infinite range, at least within the assumption of single-mode perturbation.

The mechanism for soliton crystallization that we observe is a synthesis of and elaboration upon previously reported phenomena. It has been shown that local interactions between cavity solitons can arise through decaying oscillatory tails[39], leading to the formation of small, locally ordered soliton molecules. Furthermore, it has been shown that the injection of an additional c.w. laser into a passive fibre-ring resonator can result in the generation of uniform distributions of solitons[40], and this can be viewed as a c.w.–soliton interaction. In our experiments, the 'injected' c.w. laser is provided naturally by the solitons themselves.

As one specific example of spontaneous crystallization driven by the extended background wave, the spectrum in the bottom of Fig. 1d exhibits excess power near optical modes $5 \times 24 = 120$ (1,547 nm) and $7 \times 24 = 168$ (1,541 nm), counted from the pump laser. Also visible is suppressed comb generation where the comb–resonator detuning has been increased. Here 24 FSRs is the spacing of the prominent primary-comb lines arising from the modulation instability phase-matching condition, and 24 is approximately the maximum number of soliton pulses that can be seeded into the resonator. A phenomenological application of coupled-mode theory[41] could be used to calculate the spectrum of the solitons perturbed by the mode crossing, but we find that to explain the existence of this 23-soliton crystal and the apparently exact circumferential spacing of the pulses by $2\pi/24$ radians, it is sufficient to incorporate into the LLE a reduced comb–resonator detuning on only mode 120 or on mode 168, where the excess power is largest. The crystal is then a steady-state solution of the resulting perturbed LLE.

A superstructured spectrum and contrast with the soliton liquid. With the above understanding of soliton crystallization in place, we can consider a range of crystal configurations that can be explained through this universal model. To begin, we consider a second crystal spectrum, shown in Fig. 2, which was first reported by Del'Haye and co-authors[32]. This crystal exhibits superstructure—the soliton train is nearly periodic in a small unit cell but is modulated with a larger periodicity. This results from the frustrated uniform distribution of 16 solitons with allowed inter-soliton separations of $2\pi n/49$ rad; one pair is spaced by $4 \times 2\pi/49$ rad instead of $3 \times 2\pi/49$ rad. Excess power is apparent in the spectrum at mode 49 (highlighted by the red circle in the plot) and we simulate this crystal by phenomenologically reducing the comb–resonator detuning on mode 49 so that the experimental and simulated spectra agree. The background wave

resulting from the constructive interference of the extended waves of the solitons, each with an angular period of $2\pi/49$ rad, is visible in the plots of the simulated intensity in Fig. 2b,c.

To gain insight into crystal generation, we simulated laser frequency scans across the resonance that generates this crystal in the presence of the mode crossing on mode 49. Example scans are shown for the case without the mode crossing (green) and with it (blue) in Fig. 2d. In both scans, solitons emerge from chaos as the frequency of the laser is decreased. In the presence of the mode crossing, they are generated with inter-soliton separations of $2\pi n/49$ rad. A greater number of solitons emerge from chaos in the presence of the mode crossing, and this higher number helps to stabilize the crystal against thermal changes in the experiment. Furthermore, upon continuation of the simulation, some of the solitons in the scan without the mode crossing interact attractively and pair-annihilate, while the crystallized ensemble resulting from the scan with the mode crossing remains stable indefinitely.

We investigated the pair-distribution function (PDF) for the soliton ensembles generated by these scans. The PDF is the probability that a soliton exists at position $\theta_o + \Delta\theta$, given that a different soliton exists at position θ_o, normalized to the density. This is a useful metric to classify particle interactions, which we borrow from condensed matter physics (see, for example, ref. [42], especially fig. 2 and ref. [43], especially fig. 1.1 and chapter 3). We note that for numerically calculated discrete PDFs the absolute scaling of the PDF is not important, as it depends on the density of numerical sampling. In Fig. 2e, we plot the average PDFs for 10,000 simulated scans with and without the mode crossing. The result for the case with a mode crossing is sharply peaked, indicating that the allowed inter-soliton separations take on discrete values. The result for the case without the mode crossing is continuous, with a peak near the most likely nearest-neighbour separation and periodic revivals at its multiples, falling to the value of the PDF for uncorrelated soliton positions (the density) at large separations. This is exactly the expected form of the PDF for a liquid[42,43]. For comparison, we plot a PDF (black, Fig. 2e) generated by simulation of a simple particle ensemble with a mean inter-particle separation of $\Delta\theta = 0.155\pi$ and normally distributed noise on this value with a standard deviation of $\sigma_{\delta\theta} = 0.18\Delta\theta$. Thus, with a particle labelled by $n=0$ fixed at $\theta = 0$, the position of particle n is $\theta_o = n\Delta\theta + \Sigma^n \delta\theta_i$, where $\delta\theta_i$ are the instances of the random variable representing the noise on the pulse spacings.

Soliton crystal configuration space. We observe a rich variety of soliton crystals explained by ordering in accordance with an extended background wave as described above. Many of the optical spectra are plotted in Fig. 3. Operationally, we adjust the pump laser power to provide repeatable conditions for creating particular crystals. More complex crystals occur with increased laser power, which intensifies the fluctuations in the chaos that precedes crystal generation and provides less well-ordered initial conditions. Once a crystal is generated, it is stable to small adjustments in the pump power and detuning, as the crystal structure is determined by the initial conditions for soliton formation rather than by an explicit dependence on pump power or detuning. The crystals we observe exhibit vacancies (Schottky defects)[27], Frenkel defects[27], disorder, or superstructure, or some combination thereof. A Frenkel defect consists of the shifting of a soliton in an otherwise uniform crystal. Disordered crystals are crystals in which the solitons fall on the peaks of the extended background wave, but their distribution across these peaks varies without any apparent regular order or favoured period.

We highlight the crystal plotted in Fig. 3n. This crystal exhibits both superstructure, with a superlattice period of $2\pi/3$ rad, and a Frenkel defect. Three identical supercells per resonator roundtrip yield a spectrum that has light in optical modes spaced by three resonator FSRs, because the waveform's period has been reduced threefold. The Frenkel defect, occurring once per roundtrip, contributes
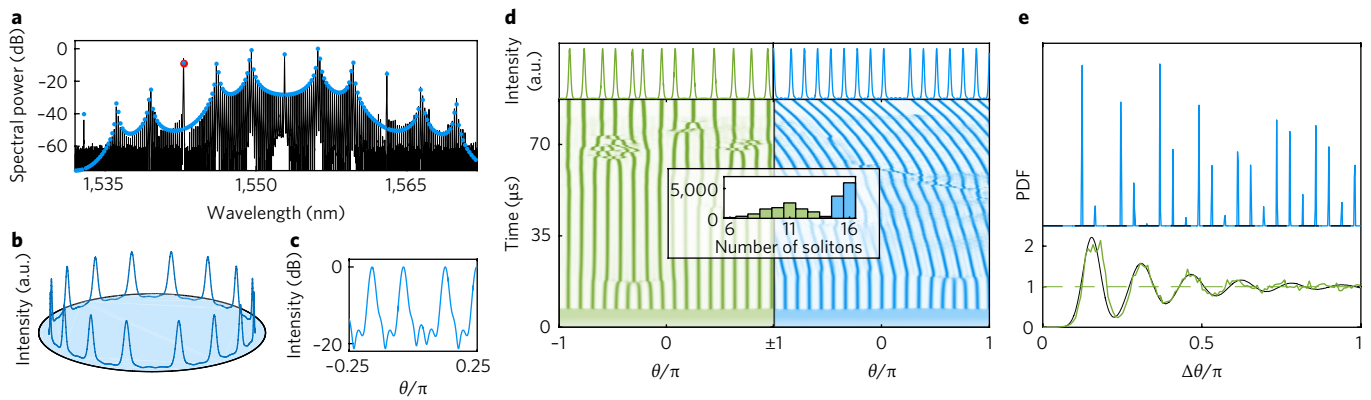
Fig. 2 | Investigation of a superstructured crystal. a, Experimental (black) and simulated (blue) optical spectra, with the red circle indicating the mode crossing discussed in the text. **b,c**, Simulated time-domain power of 16 nearly uniformly distributed solitons, corresponding to the simulated spectrum in **a**, on linear (**b**) and logarithmic (**c**) scales. **d**, Bottom: plots of the intracavity power during a simulated scan across the resonance, without (green) and with (blue) a mode crossing. Top: final waveforms. Inset: histogram of the number of solitons generated in 10,000 simulated scans. **e**, Average pair-distribution functions (PDFs) for 10,000 simulated scans across the resonance with (blue) and without (green) a mode crossing. The width of the peaks in the discrete PDFs is a single $\Delta\theta$ bin. The expected PDF of a simple one-dimensional liquid (see main text) is plotted for comparison (black).
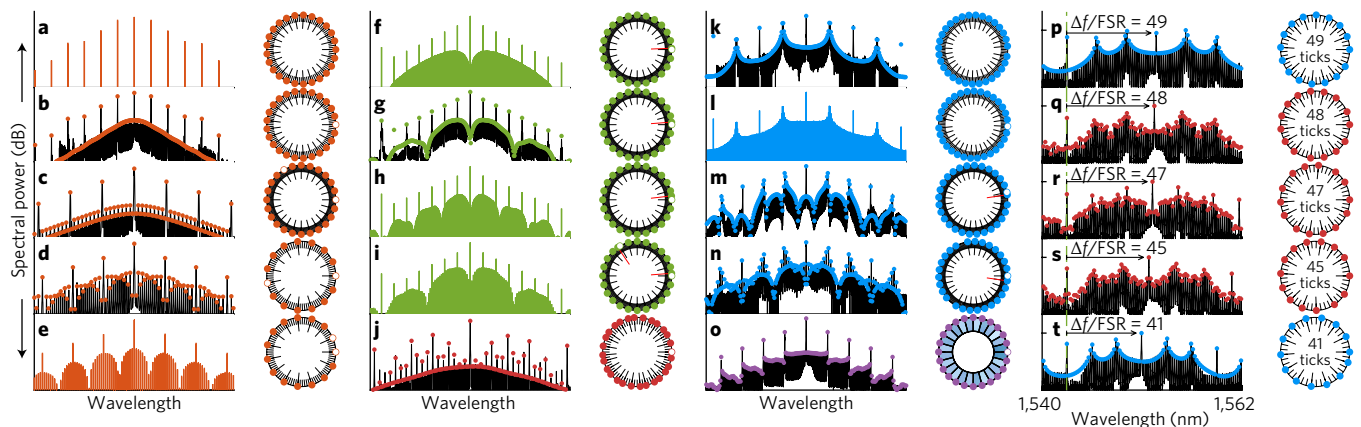
Fig. 3 | A taxonomy of soliton crystals. Measured optical spectra are shown in black and simulations in colour. Schematic depictions of the soliton distribution in the resonator are shown to the right of each spectrum. Major ticks in the schematic diagrams indicate the location or expected location of a soliton. Minor ticks indicate peaks of the extended background wave due to the mode crossing. **a**, A perfect soliton crystal, consisting of 25 uniformly distributed solitons. **b–e**, Soliton crystals exhibiting vacancies. **f–i**, Soliton crystals exhibiting Frenkel defects. Shifted solitons still lie at peaks of the extended background wave. **j**, A disordered crystal. **k–n**, Crystals exhibiting superstructure. **o**, A crystal with irregular inter-soliton spacings. Darker shading indicates a smaller inter-soliton spacing. The range in inter-soliton spacings is 3% of the mean. **p–t**, A series of crystals generated as the pump laser is moved progressively closer to the stabilizing mode crossing.

the single-FSR lobes to the spectrum. The result is three bursts of 8, 9 and 10 solitons, respectively.

Figure 3o shows a soliton crystal with inter-soliton separations that are slightly irregular and which we have not simulated as a steady-state solution of any perturbed LLE. We expect that the formation of the crystal and the distribution of solitons are dictated by mode interactions, but that in this case our simple approximation of a perturbation to the LLE by a reduced comb–resonator detuning on a single comb mode is not appropriate.

Finally, we highlight the series of crystals plotted in Fig. 3p–t. This series of crystals was generated by moving the pump laser closer to a mode crossing in steps of integer multiples of the resonator FSR. These data demonstrate the influence of the background beating between the pump laser and the mode crossing in determining the configuration of solitons in the resonator.

Time-domain measurements of Kerr soliton crystallization. It is recognized in ultrafast optics that it is not generally possible to

infer the time-domain waveform of an optical signal from its power spectrum without additional information[44]. In the limit of a delta-function reference pulse, optical cross-correlation directly measures the time-domain waveform. To approximate this limit, we perform cross-correlation measurements with a reference pulse of duration comparable to that of the solitons, which allows us to precisely identify and characterize crystals and their defects. These measurements, together with our knowledge of the LLE and its solution space, confirm our interpretation of spectral data. We describe a representative measurement in the following (for details see Methods).

In Fig. 4, we plot the simulated time-domain waveforms of the reference pulse and crystal 3j (Fig. 4a), the simulated and measured cross-correlation signals (Fig. 4b) and the temporal spacing between peaks of the cross-correlation signals (Fig. 4c). We observe agreement between the measured and simulated cross-correlation signals, confirming both our generic interpretation of the spectrum as a superposition of solitons and the specific inversion of this spectrum to determine the distribution of the solitons in this
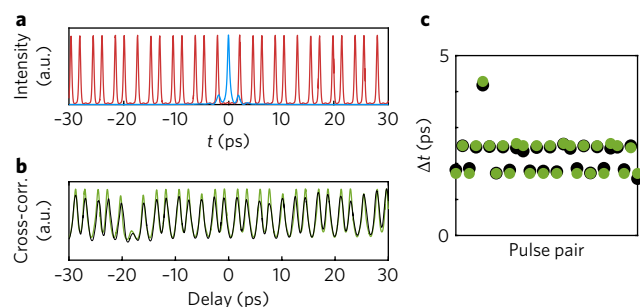
Fig. 4 | Intensity cross-correlation measurements of crystal j from Fig. 3.
a, Simulated crystal (red) and reference (blue) intensity profiles.
b, Measured (black) and simulated (green) cross-correlation signals.
The contrast between peaks of the cross-correlation signal, for both theory
and experiment, is limited by the duration and shape of the reference pulse
and increases between soliton pairs with larger temporal separations.
c, Temporal separations between adjacent peaks for the measured (black) and
simulated (green) cross-correlation signals. Mean fractional error is 3.5%.

disordered crystal. Beyond confirming our interpretation of the
data, the cross-correlation measurement represents the incorpora-
tion of a new tool into the repertoire of techniques available for
investigating Kerr combs.

Discussion

Our observation and explanation of spontaneous soliton crystal-
lization in monolithic Kerr resonators advances the field of micro-
combs by exploring microcomb soliton physics in a new tightly
packed regime, and it demonstrates that adiabatic soliton genera-
tion is possible in these systems with the help of avoided mode
crossings. A major benefit of using soliton crystals for microcomb
applications is the enhanced efficiency P_{comb}/P_{pump} of these combs,
because P_{comb} scales linearly with the number of solitons co-circu-
lating in the resonator, each of which converts a fixed amount of
power from the pump to the comb while preserving the level of
the c.w. background. Soliton crystallization in Kerr resonators sug-
gests a new route for customizability of frequency-comb spectra
and time-domain waveforms through engineering of mode interac-
tions[4,37]. An important note for applications is that the bandwidth
of a soliton crystal is determined by the bandwidth of its constituent
solitons, which are identical, independent excitations with proper-
ties determined by the resonator; thus, broadband soliton crystals
could be generated through engineering of a suitable resonator
dispersion profile, as has been demonstrated for single- and few-
soliton ensembles[11,12]. Our work and other theoretical work[38,40] sug-
gest that it may be possible to use a mode crossing or a bichromatic
pump to generate a seed crystal for creating complex, custom soli-
ton trains, which could be populated through the use of a pulsed
pump laser. Potential applications of the storage and manipula-
tion of solitons in nonlinear resonators have attracted considerable
interest[13–16,29,45], and soliton crystals in monolithic Kerr resonators
present a possible mechanism for chip-integrated optical data stor-
age and manipulation that exploits the enormous degeneracy of
soliton crystal configuration space. We expect that soliton crys-
tals possess greater stability to environmental fluctuations than
other soliton ensembles, and this is a promising avenue for further
research. Finally, we point out that it would be interesting if future
work could experimentally probe the soliton crystallization phase
transition by tuning the coupling between the degenerate resona-
tor modes responsible for crystallization, and it would be worth
exploring the relationship between self-organized soliton crystals
and manifestly quantum fluids of light with interactions arising
through optical nonlinearity[46].

Methods

Methods, including statements of data availability and any associated
accession codes and references, are available in the online version
of this paper.

References

1. Kippenberg, T. J., Holzwarth, R. & Diddams, S. A. Microresonator-based
   optical frequency combs. *Science* **332**, 555–559 (2011).
2. Diddams, S. A. The evolving optical frequency comb. *J. Opt. Soc. Am. B* **27**,
   B51–B62 (2010).
3. Herr, T. et al. Temporal solitons in optical microresonators. *Nat. Photon.* **8**,
   145–152 (2014).
4. Herr, T. et al. Mode spectrum and temporal soliton formation in optical
   microresonators. *Phys. Rev. Lett.* **113**, 123901 (2014).
5. Joshi, C. et al. Thermally controlled comb generation and soliton
   modelocking in microresonators. *Opt. Lett.* **41**, 2565–2568 (2016).
6. Yi, X., Yang, Q.-F., Yang, K. Y., Suh, M.-G. & Vahala, K. Soliton frequency
   comb at microwave rates in a high-Q silica microresonator. *Optica* **2**,
   1078–1085 (2015).
7. Drake, T. E. et al. An octave-bandwidth Kerr optical frequency comb on a
   silicon chip. *Adv. Opt. Photon.* STu3Q.4 (2016).
8. Godey, C., Balakireva, I. V., Coillet, A. & Chembo, Y. K. Stability analysis of
   the spatiotemporal Lugiato–Lefever model for Kerr optical frequency combs
   in the anomalous and normal dispersion regimes. *Phys. Rev. A* **89**,
   063814 (2014).
9. Coen, S., Randle, H. G., Sylvestre, T. & Erkintalo, M. Modeling of octave-
   spanning Kerr frequency combs using a generalized mean-field Lugiato–
   Lefever model. *Opt. Lett.* **38**, 37–39 (2013).
10. Coen, S. & Erkintalo, M. Universal scaling laws of Kerr frequency combs.
    Opt. Lett. **38**, 1790–1792 (2013).
11. Yang, K. Y. et al. Broadband dispersion-engineered microresonator on a chip.
    Nat. Photon. **10**, 316–320 (2016).
12. Okawachi, Y. et al. Bandwidth shaping of microresonator-based frequency
    combs via dispersion engineering. *Opt. Lett.* **39**, 3535–3538 (2014).
13. Jang, J. K., Erkintalo, M., Coen, S. & Murdoch, S. G. Temporal tweezing of
    light through the trapping and manipulation of temporal cavity solitons. *Nat.
    Commun.* **6**, 7370 (2015).
14. Leo, F. et al. Temporal cavity solitons in one-dimensional Kerr media as bits
    in an all-optical buffer. *Nat. Photon.* **4**, 471–476 (2010).
15. Jang, J. K. et al. All-optical buffer based on temporal cavity solitons operating
    at 10 Gb/s. *Opt. Lett.* **41**, 4526–4529 (2016).
16. Jang, J. K., Erkintalo, M., Murdoch, S. G. & Coen, S. Ultraweak long-range
    interactions of solitons observed over astronomical distances. *Nat. Photon.* **7**,
    657–663 (2013).
17. Coillet, A. et al. Azimuthal Turing patterns, bright and dark cavity solitons in
    Kerr combs generated with whispering-gallery-mode resonators. *IEEE
    Photon. J.* **5**, 6100409 (2013).
18. Renninger, W. H. & Rakich, P. T. Closed-form solutions and scaling laws for
    Kerr frequency combs. *Sci. Rep.* **6**, 24742 (2016).
19. Qi, Z., D'Aguanno, G. & Menyuk, C. R. Nonlinear frequency combs generated
    by cnoidal waves in microring resonators. *J. Opt. Soc. Am. B* **34**, 785–794 (2017).
20. Malomed, B. A., Schwache, A. & Mitschke, F. Soliton lattice and gas in
    passive fiber-ring resonators. *Fiber Integr. Opt.* **17**, 267–277 (1998).
21. Mitschke, F. & Schwache, A. Soliton ensembles in a nonlinear resonator. *J.
    Opt. B* **10**, 779–788 (1998).
22. Schwache, A. & Mitschke, F. Properties of an optical soliton gas. *Phys. Rev. E*
    55, 7720–7725 (1997).
23. Zajnulina, M. et al. Characteristics and stability of soliton crystals in optical
    fibres for the purpose of optical frequency comb generation. *Opt. Commun.*
    393, 95–102 (2017).
24. Haboucha, A., Leblond, H., Salhi, M., Komarov, A. & Sanchez, F. Coherent
    soliton pattern formation in a fiber laser. *Opt. Lett.* **33**, 524–526 (2008).
25. Amrani, F., Salhi, M., Grelu, P., Leblond, H. & Sanchez, F. Universal soliton
    pattern formations in passively mode-locked fiber lasers. *Opt. Lett.* **36**,
    1545–1547 (2011).
26. Haboucha, A., Leblond, H., Salhi, M., Komarov, A. & Sanchez, F. Analysis of
    soliton pattern formation in passively mode-locked fiber lasers. *Phys. Rev. A*
    78, 043806 (2008).
27. Ashcroft, N. W. & Mermin, D. N. *Solid State Physics* (Brooks Cole, Belmont,
    USA, 1976).
28. Herr, T. et al. Universal formation dynamics and noise of Kerr-frequency
    combs in microresonators. *Nat. Photon.* **6**, 480–487 (2012).
29. McDonald, G. S. & Firth, W. Spatial solitary wave optical memory. *J. Opt.
    Soc. Am. B* **7**, 1328–1335 (1990).

30. Luo, K., Jang, J. K., Coen, S., Murdoch, S. G. & Erkintalo, M. Spontaneous creation and annihilation of temporal cavity solitons in a coherently driven passive fiber resonator. *Opt. Lett.* **40**, 3735–3738 (2015).
31. Del'Haye, P., Beha, K., Papp, S. B. & Diddams, S. A. Self-injection locking and phase-locked states in microresonator-based optical frequency combs. *Phys. Rev. Lett.* **112**, 043905 (2014).
32. Del'Haye, P. et al. Phase steps and resonator detuning measurements in microresonator frequency combs. *Nat. Commun.* **6**, 5668 (2015).
33. Del'Haye, P., Diddams, S. A. & Papp, S. B. Laser-machined ultra-high-*Q* microrod resonators for nonlinear optics. *Appl. Phys. Lett.* **102**, 221119 (2013).
34. Lee, H. et al. Chemically etched ultrahigh-*Q* wedge-resonator on a silicon chip. *Nat. Photon.* **6**, 369–373 (2012).
35. Silver, J. M., Guo, C., Del Bino, L. & Del'Haye, P. Kerr superoscillator model for microresonator frequency combs. *Phys. Rev. A* **95**, 033835 (2017).
36. Carmon, T., Yang, L. & Vahala, K. J. Dynamical thermal behavior and thermal self-stability of microcavities. *Opt. Express* **12**, 4742–4750 (2004).
37. Liu, Y. et al. Investigation of mode coupling in normal-dispersion silicon nitride microresonators for Kerr frequency comb generation. *Optica* **1**, 137–144 (2014).
38. Hansson, T. & Wabnitz, S. Bichromatically pumped microresonator frequency combs. *Phys. Rev. A* **90**, 013811 (2014).
39. Skryabin, D. V. & Firth, W. J. Interaction of cavity solitons in degenerate optical parametric oscillators. *Opt. Lett.* **24**, 1056–1058 (1999).
40. Wabnitz, S. Control of soliton train transmission, storage, and clock recovery by CW light injection. *J. Opt. Soc. Am. B* **13**, 2739–2749 (1996).
41. Haus, H. A. & Huang, W. Coupled-mode theory. *Proc. IEEE* **79**, 1505–1518 (1991).
42. Barker, J. A. & Henderson, D. What is 'liquid'? Understanding the states of matter. *Rev. Mod. Phys.* **48**, 587–671 (1976).
43. Egami, T. & Billinge, S. *Underneath the Bragg Peaks* (Elsevier, Oxford, UK, 2012).
44. Weiner, A. *Ultrafast Optics* (Wiley, Hoboken, USA, 2009).
45. Pang, M., He, W., Jiang, X. & Russell, P. S. J. All-optical bit storage in a fibre laser by optomechanically bound states of solitons. *Nat. Photon.* **10**, 454–458 (2016).
46. Carusotto, I. & Ciuti, C. Quantum fluids of light. *Rev. Mod. Phys.* **85**, 299–366 (2013).
47. Spillane, S. M., Kippenberg, T. J., Painter, O. J. & Vahala, K. J. Ideality in a fiber-taper-coupled microresonator system for application to cavity quantum electrodynamics. *Phys. Rev. Lett.* **91**, 043902 (2003).
48. Beha, K. et al. Electronic synthesis of light. *Optica* **4**, 406–411 (2017).

Acknowledgements

Author contributions

E.S.L., D.C.C., P.D.'H. and S.B.P. performed the crystal generation experiments. D.C.C. analysed the data, developed the model, and performed the numerical simulations. E.S.L. performed the cross-correlation experiments. D.C.C. wrote the manuscript. All authors discussed the experiments and the model and contributed to revision of the manuscript.

Competing interests

The authors declare no competing financial interests.

Additional information

Supplementary information is available for this paper at doi:10.1038/s41566-017-0009-z.

Reprints and permissions information is available at www.nature.com/reprints.

Correspondence and requests for materials should be addressed to D.C.C.

Publisher's note: Springer Nature remains neutral with regard to jurisdictional claims in published maps and institutional affiliations.

Methods

Crystal generation. Soliton crystals were generated in 16.5 GHz FSR disk[34] and 26 GHz FSR rod[33] silica resonators. The disk resonator has an anomalous dispersion of ~5 kHz per mode, and the rod resonator is described in ref. [24]. For crystal generation, a telecom-wavelength pump laser (typically 1,550–1,565 nm) is coupled into a whispering-gallery mode of the resonator using a tapered optical fibre[47] and scanned with decreasing optical frequency across the resonance. A sawtooth-shaped frequency scan is used, with a period between 10 ms and 1 s. The scan range is typically on the order of 3 GHz, for scan rates from 3 to 300 GHz s^{-1}. Soliton crystals can also be generated by scanning the pump frequency arbitrarily slowly by hand. The pump laser's power is set to between 2.5 and 6 times the measured absolute threshold power for parametric oscillation, typically resulting in 30–80 mW power input to the taper. To measure the optical spectrum of primary comb, chaos or soliton crystal, the frequency scan is stopped at an appropriate point where the desired state exists. During the laser scan, the resonator absorbs the laser power and heats up, leading to an increase in the resonant wavelength due to thermo-optic effects that increase the optical path length. This results in a triangular, rather than Lorentzian, lineshape as the laser frequency is decreased[36], a greatly increased resonance linewidth and a hysteretic lineshape that is dependent upon the direction of the scan.

Diagnostics collected during crystal generation include the optical power transmitted through the tapered fibre, this same power with the pump frequency removed using a spatial light modulator or optical band-reject filter, and the repetition-rate signal of the generated optical waveform collected by a 50 GHz photodiode.

Because crystal generation relies on a coupling between nominally orthogonal mode families in the resonator, it is sensitive to the position of the tapered optical fibre. The taper contacts the resonator and provides the coupling between mode families. The optimum taper position for crystal generation, in terms of position within the plane perpendicular to propagation and position along the taper's axis, is determined experimentally.

Numerical simulations. For technical details of the numerical simulations performed for this work, see Supplementary Sections I and II.

Simulation of soliton crystals. The simulation of a soliton crystal exploits two independent experimental observations that are mutually confirmatory. First, the time-domain pulse train is deduced from the complicated shape of the optical spectrum of a soliton crystal by beginning with the assumption that the spectrum arises from a superposition of solitons, with no invocation of the crystallization theory we have presented above. A simple example is the pulse train corresponding to the 'primary-comb-plus-soliton' spectrum in Fig. 1d, in which a soliton is added out of phase to a uniform soliton pulse train with a primary-comb-like spectrum. This soliton contributes the underlying single-FSR spectral envelope and eliminates a soliton from the pulse train in the time domain. Crystals with Frenkel defects may be understood in this way as well: the lobed structure in the spectrum is due to the spectral interference between an out-of-phase soliton which is added to the pulse train to remove a soliton as above and an in-phase soliton which is added to yield the shifted pulse.

Once the pulse train corresponding to the general structure of the spectrum has been deduced, the experimental spectrum can be compared to the spectrum of this pulse train calculated as a simple superposition of sech^2 pulses. This comparison reveals localized excess power in the experimental spectrum, which is evidence of a mode crossing. The strength of the mode crossing, controlled in the experiment by the taper-induced coupling between the modes, is determined phenomenologically from the magnitude of the excess power and reduced comb–resonator detuning on a single optical mode is incorporated into a perturbed LLE as described in the Supplementary Information. It is then verified that the pulse train whose spectrum matches the experimental data is a steady-state solution to this perturbed LLE, which requires the inter-soliton separations to be multiples of the period of the beat between the excess power and the pump laser. This period is $2\pi/\mu_x$, where μ_x is the mode number at the crossing. This process connects the presence of excess power on a single optical mode of the spectrum to the general shape of the spectrum, two observations that are not related a priori.

This process is applied for all of the crystal states presented in Fig. 3 except for the disordered crystals and the crystal in Fig. 3o. For 10 of the 13 experimental crystal spectra to which we applied the model, the stabilizing mode crossing is visible in the data but not necessarily shown in the figure. For the other three the position of the mode crossing is inferred from the distribution of solitons and other crystal states observed in the same resonator. To model the disordered crystals, the pulse train is not deduced from the shape of the optical spectrum. Instead, excess power due to a mode crossing is identified through the presence of an asymmetry in the spectrum about the pump. The location of the excess power then fixes the allowed inter-soliton separations in the resonator, after which an exhaustive search is performed until a pulse train is found that yields the experimental spectrum. As described in the text, we have not simulated spectrum 3o as a steady-state solution to any perturbed LLE, which we expect is because the crystal is stabilized by a more complex spectrum of excess power.

Instability of soliton crystals under the LLE. None of the crystals we present are steady-state solutions to the unperturbed LLE. To arrive at this conclusion, we note that the temporal width of the pulses is determined by the bandwidth of the spectrum. This sets a lower bound on the range of their attractive interactions, which is too large for any of the crystals to be stable.

In Supplementary Fig. 4 we demonstrate the crystallization of an initially non-uniform pulse train due to the presence of a mode crossing, as well as the instability of the same pulse train without the mode crossing to stabilize it.

Cross-correlation measurements. Supplementary Fig. 1 presents a schematic depiction of the cross-correlation measurements, for which we use a commercial optical cross-correlator with a LiIO$_3$ crystal. We use for a reference pulse the output of an electro-optic comb generator[48] whose repetition rate is locked to the repetition rate of the ~16.5 GHz crystal pulse train and which is generated from the same pump laser. When the reference pulse and the soliton crystal pulse train are sent together into the nonlinear crystal exhibiting the χ_2 nonlinearity at 90° angles to each other, an amount of light proportional to the product of their intensities, at the sum of their frequencies, is emitted in a third direction. By measuring the average power of this emitted light while scanning the relative delay, we measure the intensity cross-correlation between the crystal and the reference pulse.

We operated our experiment in a through-coupled configuration, which results in destructive interference between the outcoupled solitons and the through-coupled pump. The solitons manifest as dips in the through-coupled intensity, resembling so-called dark solitons[8]. To correct this we use a spatial light modulator to rotate the phase of the pump laser by π so that it constructively interferes with the solitons, yielding solitons riding on top of a c.w. background. This c.w. background is larger than the c.w. background that exists inside the cavity because it arises from the pump laser, which is transmitted past the resonator.

The simulated cross-correlation signal is sensitive to the intensity profile of the reference pulse. We can measure only its intensity autocorrelation, which we combine with our knowledge of its production to estimate the intensity profile. To demonstrate that the validity of the results we present here does not depend on the exact assumptions we make about the intensity profile, we have also simulated the intensity cross-correlation resulting from an assumed Gaussian reference pulse with the same autocorrelation width as is measured for the reference pulse. The resulting simulated cross-correlation does not qualitatively agree as well with the experimental data in the depths of the wells between peaks, because it does not contain satellite pulses that contribute to the variations in this depth, but the quantitative comparison of the temporal spacing between peaks is similar: the mean (maximum) normalized error between experiment and theory is 3.5% (9.1%) for the assumed electro-optic comb pulse and 4.8% (10.6%) for the Gaussian pulse.

Data availability. The data that support the plots within this paper and other findings of this study are available from the corresponding author upon reasonable request.